Haze Removal for a Single Remote Sensing Image Using Low-Rank and Sparse Prior

Guoling Bi, Guoliang Si, Yuchen Zhao, Biao Qi, and Hengyi Lv

Abstract—**Due to the influence of atmospheric scattering, the quality of remote sensing images is degraded, which severely limits the utility of remote sensing images. In this article, a novel dehazing algorithm for a single remote sensing image is proposed based on a low-rank and sparse prior (LSP). According to an atmospheric scattering model, the dark channel of a hazy image is decomposed into two parts: the dark channel of direct attenuation with sparseness and the atmospheric veil with low rank. The prior is obtained from the overall decomposition of the image rather than the patches of the image; therefore, the image pixel changes of the local blocks have little influence on the prior. Considering different resolutions of remote sensing images, the calculations of blocks involved in this article are completed by adaptive methods. The principal component pursuit and alternating direction multiplier method (PCP-ADMM) combined with the adaptive threshold shrinkage method are used for low-rank and sparse decomposition, therefore, the coarse estimation of the atmospheric veil is obtained. The guided filter with adaptive radius is used to refine it, and then the accurate atmospheric light is estimated. Finally, using the deformed atmospheric scattering model based on the atmospheric veil and atmospheric light, the haze-free image is restored. Extensive experimental results on publicly available data sets show that the dehazed images have abundant detail, high contrast, and minimal color distortion when using the proposed method, which is competitive with most state-of-the-art technologies.**

Index Terms—**Atmospheric veil, dark channel, haze removal, low-rank and sparse prior (LSP), remote sensing image.**

I. Introduction

WITH the development of remote sensing technology, both military and civilian remote sensing satellites provide a large number of remote sensing images with various ground sample distances (GDSs). These remote sensing images have been widely used in various Earth surface observation applications [1]–[3]. However, visible cameras on satellites capture electromagnetic signals far away from the Earth's surface through the atmosphere, and the quality of remote sensing images is easily affected by adverse atmospheric conditions such as haze, fog, smoke, and clouds. Even in sunny weather, the atmosphere cannot be absolutely free of any particles, therefore, haze still exists, which reduces the intelligibility and availability of remote sensing images. Therefore, dehazing for remote sensing images is a crucial and indispensable preprocessing task.

To improve the quality of remote sensing images, enhancement methods have been extensively studied. These include histogram equalization [4], [6], the homographic filter, and retinex-based methods [7], [8]. These image enhancement methods often introduce gradient reversal artifacts and oversaturation without knowing the mechanism of image degradation.

In recent years, an increasing number of prior-based dehazing methods specifically for remote sensing images have been proposed [10]–[14]. Zhang *et al.* [12] developed a haze-optimized transformation (HOT) that established a clear sky line through the high correlation between the blue and red bands and separated clouds and haze from the normal surface. Chavez [10] proposed an improved dark-object subtraction (DOS) technique to predict the haze values for all spectral bands based on the haze value of the starting band. Jiang *et al.* [13] presented an effective method based on the HOT and DOS for haze or thin cloud removal in visible remote sensing images. Makarau *et al.* [11] developed the DOS prior to obtaining a haze thickness map (HTM) for inhomogeneous haze detection and removal in multispectral remote sensing images. A ground radiance suppressed HTM (GRS-HTM) [14] was proposed to accurately estimate the haze distribution of each band of remote sensing images to restore clear images.

More recently, deep-learning-based methods have achieved great success in natural image dehazing [15]–[19], [23], [59], [60]. These methods include multiscale convolutional neural network DehazeNet [15], AOD-Net [17], the densely connected pyramid-dehazing network (DCPDN) [18], generative adversarial networks (GANs) [16], the enhanced pix2pix dehazing network (EPDN) [19], and multiscale boosted dehazing network (MSBDN) [59]. The deep-learning-based framework has also been applied to remote sensing image dehazing [20]–[22]. Hu *et al.* [21] proposed an edge-sharpening cycle-consistent adversarial network, which was an unsupervised remote-sensing image dehazed method based on cycle GANs. Gu *et al.* [22] proposed a prior-based dense attentive dehazing network (DADN) based on dense blocks and attention blocks for remote sensing image dehazing. However, due to the limitations of remote sensing image training data sets, these learning-based methods cannot adapt to various practical environments.

In RGB space, the visible band of remote sensing images has the same imaging waveband as that of natural

Manuscript received July 11, 2021; revised October 15, 2021 and November 12, 2021; accepted December 13, 2021. Date of publication December 15, 2021; date of current version March 1, 2022. This work was supported by the National Natural Science Foundation of China under Grant 61801455.
(Corresponding author: Guoling Bi.)

The authors are with the Changchun Institute of Optics, Fine Mechanics and Physics, Chinese Academy of Sciences, Changchun 130033, China (e-mail: bigl_ciomp@163.com; siguoliang@163.com; zhao_yc@163.com; qibiao@163.com; hengyi_lv@163.com).

Digital Object Identifier 10.1109/TGRS.2021.3135975

images; therefore, the dehazing of remote sensing images can also refer to successful dehazing methods of natural images [24]–[26], [28]–[32]. Berman *et al.* [29] proposed the nonlocal prior (NLD) for single-image dehazing. In RGB space, the algorithm assumed that a haze-free image can be represented by a few hundred tight color clusters. Zhu *et al.* [28] proposed the color attenuation prior (CAP) recovering the scene depth of a hazy image. He *et al.* [25] proposed the famous dark channel prior (DCP) in which most local patches in haze-free images contain some pixels that have quite low intensities in at least one color channel. Then, many DCP-based methods were proposed [9], [33]–[35]. Long *et al.* [33] presented a fast and effective method based on DCP for single remote sensing image dehazing that automatically extracts global atmospheric light and refined atmospheric veils. Xu *et al.* [35] proposed DCP-based iterative dehazing for remote sensing images (IDeRS). The virtual depth was defined, and a fusion model was proposed for combining pixelwise and patchwise transmission map estimations. Bui *et al.* [32] proposed the color ellipsoid prior (CEP), which found patches locally that can maximize the color contrast in a hazy image. Although these prior-based methods achieved promising results, the dehazing quality often depends on the conformity between the proposed prior and real data. Inspired by CEP [32], Guo *et al.* [34] proposed an elliptical boundary prior (EBP) for remote sensing images in which changes in the elliptical boundary in haze can be used to assess the haze thickness of pixels in a patch.

However, there are some differences between remote sensing images and natural images, which affect the adoption of dehazing methods. First, atmospheric light is usually estimated by the sky region of natural images, but remote sensing images do not contain sky regions. Second, the density of haze changes with the depth of field of natural images. However, due to the large distance of remote sensing imaging, the depth of the field of remote sensing images can be regarded as a constant. Finally, remote sensing images usually have GDSs ranging from tens of centimeters to tens of meters, while natural images usually have similar resolutions and scales. Although some natural image dehazing methods have been successfully applied to haze removal for remote sensing images, the large differences between natural images and remote sensing images should be fully considered to achieve the best performance.

From the above analysis, it can be seen that most of the current algorithms are patch-based [23], [25], [32], [34], which usually perform dehazing with a fixed patch size. For remote sensing images, the resolution is not the same, and using the same size also leads to unclear details or halo artifacts. In addition, for a prior-based dehazing method, when the local patch of the image does not conform to the prior, the prior is invalid, resulting in color distortion, insufficient dehazing, and oversaturation in the dehazed images.

Different from the existing methods, according to the characteristics of different resolutions of remote sensing images without sky region and by comprehensively considering the direct attenuation model and atmospheric light model in an atmospheric scattering model, a dehazing method is proposed for a single remote sensing image. We propose a robust low-rank and sparse prior (LSP), which is obtained from the overall decomposition of the image rather than the patches of the image; therefore, the image pixel changes of the local blocks have little influence on the prior. Considering the different resolutions of remote sensing images, the calculations of blocks involved in this article are completed by adaptive methods. Therefore, the proposed method is not affected by the remote sensing image resolution or local pixel changes and has good robustness. The dehazed images have high contrast, rich detail, minimal color distortion, and few halo artifacts.

The main contributions of this article are summarized as follows:

1) Based on an atmospheric scattering model, the dark channel of the hazy image is decomposed into a direct-attenuation dark channel and atmospheric veil. It is verified that the direct-attenuation dark channel is sparse, while the atmospheric veil is low rank; therefore, the problem of dehazing is transformed into a problem of low-rank and sparse decomposition, which makes the prior more robust.
2) The adaptive patch sizes of dark channel pixels are used to ensure the sparsity of the patch, and the adaptive patch size is used as the radius of the guided filter.
3) An adaptive threshold shrinkage method is introduced. Called principal component pursuit and alternating direction multiplier method (PCP-ADMM), this method is used for low-rank and sparse decomposition to obtain the coarse estimation of the atmospheric veil, and a guided filter with adaptive radius is used to refine it.
4) Considering that there is no sky region in remote sensing images, according to the physical meaning of atmospheric veils, we use the refined atmospheric veil to estimate atmospheric light.

The rest of this article is organized as follows. In Section II, we describe the related work. The proposed algorithm is presented in Section III. Section IV gives the experimental settings, results, and analysis, followed by a conclusion in Section V.

II. Related Work

The atmospheric scattering model [27] is typically used to describe the impact of bad weather conditions such as haze and fog on images. This model is depicted as

$$I(x) = J(x)t(x) + A(1 - t(x)) \tag{1}$$

where x is the pixel index, $I(x)$ is the hazy image, $J(x)$ is the haze-free image, and $t(x)$ is the transmission, which indicates that the portion of the light reaches the camera without scattering. A is the global atmospheric light. The degradation model for a remote sensing hazy scene is shown in Fig. 1.

The degradation model is divided into two parts [26]. The first part $J(x)t(x)$ is called direct attenuation, which describes the weakened incident light that is not scattered and absorbed when entering the imaging system. It submerges the details and color information and reduces the contrast of images, as shown

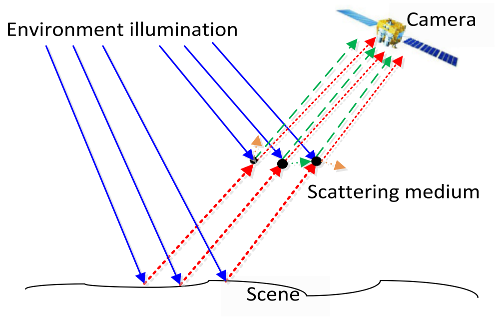

Fig. 1. Degradation model for remote sensing hazy scene.

by the red dotted line in Fig. 1. The second part $A[1 - t(x)]$ is called airlight, which results from previously scattered light and leads to the shift of the scene color, as shown by the green dotted line in Fig. 1.

Single image dehazing restores a haze-free ImageJ(x) from a hazy (x), which is an underconstrained problem. Kinds of hand-crafted priors [24]–[32], [36] are used to constrain the physical model to obtain the estimations of the transmission and atmosphere light to restore the haze-free image. For example, the CAP [28] is used to obtain the depth map of the hazy image and then estimate the transmission. The NLD [29] is used to obtain the haze lines, which can obtain a per-pixel estimation of the transmission. The DCP [25] is used to estimate the transmission map. Although the prior is invalid when the region is similar to atmospheric light and there is no shadow coverage, resulting in color distortion or some artifacts in dehazed images, DCP is still a simple and effective dehazing prior. In addition, some deep neural networks [23], [38] also fuse this prior. Chen *et al.* [23] designed a patch map selection network (PMS-Net) to select the patch size automatically for DCP dehazing. Yang *et al.* [38] proposed a novel proximal dehaze net for single-image dehazing by learning dark channels and transmission priors. It can be seen that a good prior is also very meaningful in the design of neural networks.

In addition, there have been some studies on dehazing from the perspective of an airlight model [33], [36], [37]. For example, Tarel [36] introduced the intensity of the atmospheric veil $V(x)$ to denote the air lightness of the model

$$V(x) = A(1 - t(x)). \tag{2}$$

This indicates that the atmospheric light involved in the imaging enters the field of view, causing the high-frequency components of the image to be suppressed and the low-frequency component to be highlighted, which further leads to a loss of image detail and degradation of contrast and clarity. Different from the atmospheric veil defined by Tarel [36], this value was defined by Long *et al.* [33] as

$$V(x) = 1 - t(x). \tag{3}$$

The atmospheric veil $V(x)$ is obtained by computing the minimum color channel and refined by a low-pass Gaussian filter, and then the transmission is redefined. The transmission $t(x)$ expression is

$$t(x) = e^{-\beta(x)d(x)} \tag{4}$$

where $d(x)$ is the imaging distance from the scene to the camera, which is nearly constant in remote sensing imaging, that is, $d(x) \approx d_0$. $\beta(x)$ is the scattering coefficient, which represents the attenuation of the incoming energy by aerosols, and it depends on wavelength λ and turbidity T [9]. Under haze conditions, it is usually assumed that the extinction coefficient is independent of wavelength [5]. Therefore, (4) can be written as

$$t(x) = e^{-\beta(x)d_0}. \tag{5}$$

Because the transmission $t(x) \in (0, 1]$ depends only on the pixel position and does not correspond to the wavelength, the transmissions are the same for all RGB channels [33].

III. Proposed Algorithm

Based on the atmospheric scattering model, the dark channel of a hazy image can be decomposed into a dark channel of direct attenuation with sparseness and an atmospheric veil with low rank. Therefore, we propose a haze removal method for a remote sensing image based on an LSP.

A. Model Based on Low-Rank and Sparse

Assuming the atmospheric light is known, since the transmission is the same for all RGB channels and is constant in a local patch [33], which is marked as $\tilde{t}(x)$; therefore, we perform the minimum operations on both RGB channels and the local patch in the model of (1)

$$\begin{aligned}\min_{y\in\Omega(x)}\Big(\min_{c\in\{r,g,b\}} I^c(y)\Big) \\ = \min_{y\in\Omega(x)}\Big(\min_{c\in\{r,g,b\}} J^c(y)\Big)\tilde{t}(x) + A(1 - \tilde{t}(x)).\end{aligned} \tag{6}$$

Let $I^{\text{dark}}(x) = \min_{y\in\Omega(x)}(\min_{c\in\{r,g,b\}} I^c(y))$, where $I^{\text{dark}}(x)$ is the dark channel of the hazy image. Let $J^{\text{dark}}(x) = \min_{y\in\Omega(x)}(\min_{c\in\{r,g,b\}} J^c(y))$, $J^{\text{dark}}(x)$ be the dark channel of the clear image. Equation (6) can be changed to

$$I^{\text{dark}}(x) = J^{\text{dark}}(x)\tilde{t}(x) + A(1 - \tilde{t}(x)). \tag{7}$$

Then, we can obtain the dark channel of direct attenuation as

$$D(x) = J^{\text{dark}}(x)\tilde{t}(x). \tag{8}$$

Assuming $\tilde{V}(x)$ is the coarse atmospheric veil, this can be expressed as

$$\tilde{V}(x) = A(1 - \tilde{t}(x)). \tag{9}$$

When $E(x) = I^{\text{dark}}(x)$ and $Z(x) = \tilde{V}(x)$, the hazy image model can be rewritten as

$$E(x) = D(x) + Z(x). \tag{10}$$

We refine the coarse atmospheric veil $Z(x)$ and obtain $V(x)$; then, (1) can be changed to

$$I(x) = J(x)\left(1 - \frac{V(x)}{A}\right) + V(x). \tag{11}$$

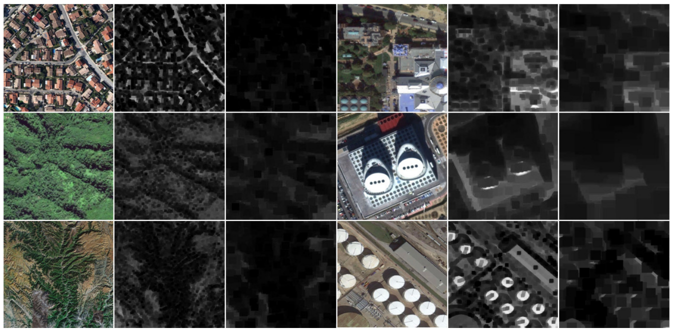

Fig. 2. Dark channels of haze-free remote sensing images with different patch sizes. (a) Haze-free images without gray areas. (b) $p = 5$. (c) $p = 15$. (d) Haze-free images with gray areas. (e) $p = 15$. (f) $p = 45$.

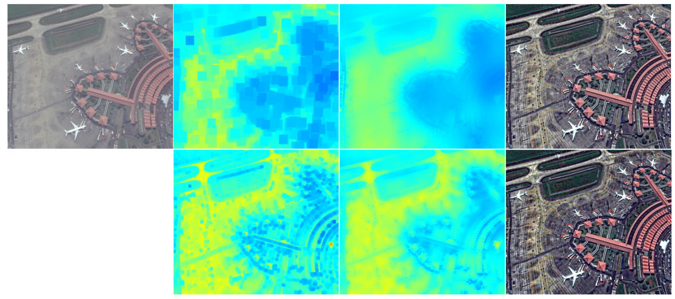

Fig. 3. Coarse and refined atmospheric veil, for the first line shows the Top: $p = r = 50$, the second line shows Bottom: $p = r = 15$. (a) Hazy remote sensing image. (b) Coarse atmospheric veil. (c) Refined atmospheric veil. (d) Dehazed results.

1) Attenuation Dark Channel Inference: Due to widespread shadows, dark objects, and colorful objects in outdoor images, the number of dark pixels increases with an increase in the minimum filtering radius when obtaining the dark channel image [56]. We select a large number of haze-free remote sensing images from remote sensing data sets for experiments, i.e., the RS_C11 database [39] and RSICD data set [40]. Here, we provide only six representative haze-free remote sensing images and their dark channel images, as shown in Fig. 2. We divide the images into two groups. For the left group, the first column on the left shows the haze-free remote sensing images without gray areas, as shown in Fig. 2(a). The second and third columns are dark channel images with patch sizes of $p = 5$ and $p = 15$, respectively. For the right group, the fourth column shows the haze-free remote sensing images with gray areas, as shown in Fig. 2(d). The fifth and sixth columns are dark channel images with patch sizes of $p = 15$ and $p = 45$, respectively.

As shown in Fig. 2, for the images without gray areas, when the patch size $p = 5$, the dark channels contain a large number of nonzero areas. When $p = 15$, the pixel values of most areas in the dark channels tend to 0; that is, the dark channel image is sparse. For the images with gray areas, when the patch size $p = x15$, there are a large number of nonzero areas in the dark channels. When $p = 45$, the pixel values of most areas in the dark channels tend to 0; that is, the dark channel image is sparse.

Some remote sensing images often contain gray and bright areas (such as the reflective area of white buildings and bright water surfaces), resulting in high values of pixels in these areas of the dark channel $J^{\mathrm{dark}}(x)$. In addition, different remote sensing images have large differences in the GDS and object scales; therefore, different patch sizes are more expected to obtain the dark channel to ensure the sparsity of dark channel images. We select a large number of remote sensing images with different GDSs for experiments. The patch size p can be approximated by counting the number of pixels in the gray area, as shown in the following equation:

$$p = \begin{cases} 15, & p < 15 \\ \mathrm{round}\left(\mathrm{sqrt}\left(\sum_{x=m}^{255} \mathrm{hist}(I(x))\right)/N\right), & \text{else} \\ 50, & p > 50 \end{cases} \quad (12)$$

where m is the minimum pixel value of the gray-white area, for 24-bit color images, we set $m = 150$. Suppose the total gray area is a square with a side length of $\mathrm{sqrt}(\sum_{x=m}^{255} \mathrm{hist}(I(x)))$, which is N times the patch size, we set $N = 5$. The round() function is the rounding operation. For a gray-white area of the same size, when the GDS is particularly large, the remote sensing image has smaller gray areas, that is, $p < 15$, and we set $p = 15$. When the GDS is small, the remote sensing image has larger gray areas, and we set $p = 50$. In this way, we realize the adaptive selection of patch size. Therefore, we can adaptively obtain the sparse dark channel of the haze-free remote sensing image. Since we know $\tilde{t}(x) \in (0, 1]$, $D(x) = J^{\mathrm{dark}}(x)\tilde{t}(x) \leq J^{\mathrm{dark}}(x)$, the dark channel of direct attenuation $D(x)$ is sparser than $J^{\mathrm{dark}}(x)$.

2) Coarse Atmospheric Veil Inference: The transmission is the same for all RGB channels, and the transmission in a local patch is constant [33]. According to (9) and (10), the coarse atmospheric veil $Z(x)$ is subject to three constraints.

1) For $\tilde{t}(x) \in (0, 1]$, $Z(x)$ is positive.
2) $Z(x)$ cannot be higher than the dark channel of the hazy image, that is $Z(x) \leq I^{\mathrm{dark}}(x)$.
3) Similar to the transmission, $Z(x)$ is constant in a local patch.

On the whole, the coarse atmospheric veil $Z(x)$ has many similar components; therefore, it has the characteristics of low rank, as shown in Fig. 3(b).

After the above analysis, it can be seen from (10) that the dark channel of a hazy image $E(x)$ can be decomposed into two parts: the dark channel of direct attenuation with sparseness and the atmospheric veil with low rank, which meet the conditions of low-rank and sparse decomposition. In this way, the image dehazing problem is converted into a problem of low-rank and sparse decomposition.

B. Low-Rank and Sparse Decomposition

Low-rank sparse decomposition (LRSD) based on the matrix kernel norm and its improved method [41]–[43] has been widely used in many fields. Candés *et al.* [41] proposed the classic principal component pursuit (PCP) method which uses the nuclear norm to approximate the rank of the matrix and uses the L1 norm to approximate the sparsity of the matrix. Therefore, (10) is transformed into an LRSD problem as follows:

$$\begin{aligned}&\min\|Z\|_* + \lambda\|D\|_1\\ &\text{s.t. } E = Z + D\end{aligned} \tag{13}$$

where $\|\|_*$ denotes the nuclear norm of the matrix, and $\|\|_1$ denotes the L1-norm, and λ is a compromise parameter that is used to balance low rank and sparse components. Usually, λ is set as $\lambda = (1)/(\max(m,n))^{1/2}$, and m is the number of rows of the image, and n is the number of columns of the image.

To obtain the optimal solution to the above-mentioned convex problem, many solving algorithms have been proposed to improve the accuracy of the solution [44]–[49]. These include the iterative thresholding (IT) algorithm [44], accelerated proximal gradient (APG) algorithm [45], primary-dual algorithm (PDA) [46], augmented Lagrange multiplier (ALM) [47], and alternating direction multiplier method (ADMM) [48], [49]. ADMM can be regarded as an attempt to combine the advantages of double decomposition and augmented Lagrangian methods for constrained optimization. ADMM takes the form of a decomposition-coordination procedure, in which the solutions to small local subproblems are coordinated to find a solution to a large global problem, which reduces the difficulty of solving large-scale problems. Therefore, we use ADMM to solve the convex optimization problem of (13). The solving process of ADMM is as follows:

The augmented Lagrangian function to (13) is

$$\begin{aligned}L\langle Z, D, Y, m\rangle = \|Z\|_* + \lambda\|D\|_1 + \langle Y, Z + D - E\rangle\\ + \frac{\mu}{2}\|Z + D - E\|_F^2\end{aligned} \tag{14}$$

where Y is a Lagrange multiplier, the operator $\langle ., .\rangle$ represents the inner product of a matrix, $\|\|_F$ represents the Frobenius norm of a matrix, and $\mu > 0$ is a penalty parameter. Next, we use ADMM to solve the optimization problem, that is, by updating one variable alternately while fixing the other variables.

1) Update Z^{k+1}: With the variables D and Y being fixed, Z can be updated by solving the following problem

$$\begin{aligned}Z^{k+1} &= \arg\min_Z L(Z, D^k, Y^k, \mu_k)\\ &= \arg\min_Z \|Z\|_* - \langle Y^k, Z + D^k - E\rangle\\ &\quad + \frac{\mu_k}{2}\left\|Z + D^k - E\right\|_F^2\\ &= \arg\min_Z \|Z\|_* + \frac{1}{2}\left\|Z - \left(E - D^k + \frac{Y^k}{\mu_k}\right)\right\|_F^2.\end{aligned} \tag{15}$$

Donohn [50] proposed the wavelet hard threshold function shrinkage method [as shown in (16)] and soft threshold function shrinkage method [as shown in (17)]. The function sign returns the sign of its operand. The threshold is set to ε. In many wavelet coefficients x, the wavelet coefficients with smaller absolute values are set to 0, and the coefficients with larger absolute values are kept or contracted

$$\widehat{x} = \begin{cases} x, & |x| \ge \varepsilon\\ 0, & |x| < \varepsilon\end{cases} \tag{16}$$

$$\widehat{x} = \begin{cases} \operatorname{sign}(x)(|x| - \varepsilon), & |x| \ge \varepsilon\\ 0, & |x| < \varepsilon.\end{cases} \tag{17}$$

However, the threshold function always has a constant deviation. To facilitate the solution of the optimal threshold and improve the efficiency of the algorithm, we propose an adaptive threshold shrinkage function $M_\varepsilon(x)$ as follows:

$$M_\varepsilon(x) = \begin{cases} \operatorname{sign}(x)\left(|x| - \varepsilon\beta^{\left(\frac{|x|}{\varepsilon} - 1\right)}\right), & |x| \ge \varepsilon\\ 0, & |x| < \varepsilon\end{cases} \tag{18}$$

where $\beta \in [0, 1]$ is an adjustment parameter. When $\beta = 0$, it becomes a hard threshold function. When $\beta = 1$, the function becomes a soft threshold function. The parameter β can adjust the approximation degree of the threshold function and the straight line $y = x$, thereby improving the efficiency of the algorithm. ε is the threshold. When $|x| \to \varepsilon$, $M_\varepsilon(x) \to 0$; when $|x| \to \infty$ and $M_\varepsilon(x) \to |x|$. With an increase in $|x|$, the deviation of $|x|$ and $M_\varepsilon(x)$ decreases, which overcomes the shortcoming of the constant deviation of the soft threshold function. We use the adaptive threshold shrinkage function (18) to update Z as follows:

$$Z^{k+1} = U M_{\frac{1}{\mu_k}}\left(\sum\right) V^T \tag{19}$$

where $[U, \sum, V] = \operatorname{svd}(E - D^k + (Y^k/\mu_k))$ and M is the adaptive threshold shrinkage function.

2) Update D^{k+1}: With variables Z and Y being fixed, D can be updated by solving the problem as follows:

$$\begin{aligned}D^{k+1} &= \arg\min_D L(Z^{k+1}, D, Y^k, \mu_k)\\ &= \arg\min_D \lambda\|D\|_1 - \langle Y^k, Z^{k+1} + D - E\rangle\\ &\quad + \frac{\mu_k}{2}\left\|Z^{k+1} + D - E\right\|_F^2\\ &= \arg\min_D \frac{\lambda}{\mu_k}\|D\|_1 + \frac{1}{2}\left\|D - \left(E - Z^{k+1} + \frac{Y^k}{\mu_k}\right)\right\|_F^2.\end{aligned} \tag{20}$$

We use the adaptive threshold shrinkage method to solve this problem as follows:

$$D^{k+1} = M_{\frac{\lambda}{\mu_k}}\left(E - Z^{k+1} + \frac{Y^k}{\mu_k}\right). \tag{21}$$

3) Update Y^{k+1} and μ_{k+1}: Update the multiplier Y and the penalty factor μ. Then,

$$Y^{k+1} = Y^k - \mu_k(Z^{k+1} + D^{k+1} - E) \tag{22}$$

$$\mu_{k+1} = \min(\sigma\mu_k, \mu_{\max}) \tag{23}$$

where $\sigma > 1$ is the magnification factor.

The termination condition of the iteration is

$$\delta = \left\|Z^{k+1} - Z^k)\right\|_F^2 < \delta_0 \tag{24}$$

where δ_0 is set to 10^{-2}.

C. Recovering the Scene Radiance

1) Refine the Coarse Atmospheric Veil: In the previous section, the low-rank atmospheric veil $\tilde{V}(x) = Z(x)$ is roughly estimated. Here, we choose one airport remote sensing image from the remote sensing data set of the RSOD database [52], as shown in Fig. 3(a). We can see that the coarse atmospheric veil has block artifacts, as shown in Fig. 3(b) (warm colors depict high values). To avoid halo artifacts in the dehazed image, a guided filter [51] is used to refine the coarse atmospheric veil, which can make the refined atmospheric veil $V(x)$ retain the structure of the original image, as shown in Fig. 3(c).

In this article, we take the adaptive patch size of the dark channel as the radius of the guided filter. According to (12), $p = 50$, therefore, the radius of the guided filter $r = 50$, as shown in the first line of Fig. 3. For comparison, we also chose $p = r = 15$ and set all of ϵ to 10^{-2} for experiments, as shown in the second line of Fig. 3.

The atmospheric veil obtained by the adaptive patch size and guided filter radius is smoother, and sufficient edge information is retained. Therefore, for the dehazed image, the color is more realistic, and there are fewer halo artifacts.

2) Estimating the Atmospheric Light: In this article, the regions with high pixel values in the refined atmospheric veil are considered to be the most haze-opaque regions, and the pixels in these regions of the hazy image $I(x)$ are used to estimate atmospheric light. We first choose the top 0.1% brightest pixels in the atmospheric veil. The regions of these brightest pixels are $\boldsymbol{\Omega}_I \in 0.1\%\{\mathrm{up}(\mathrm{count}[V(x)])\}$, and N is the total number of pixels. By calculating the averages of each channel of the hazy image $I(x)$ in these regions, the accurate atmospheric light A of the three channels is obtained as

$$A = \frac{\sum_{x \in \Omega_I} I(x)}{N}. \tag{25}$$

3) Haze Removal: The refined atmospheric veil $V(x)$ and atmospheric light are obtained according to the deformed atmospheric scattering model in (11). The haze-free scene is restored as

$$J(x) = A\frac{I(x) - \zeta V(x)}{A - \zeta V(x)} \tag{26}$$

where ζ is an adjustment factor. The image restored by (26) looks dim, and the exposure of the dehazed image is increased to display.

IV. Experimental Results

We selected remote sensing images with different haze densities, different colors, and different scenes for experiments. The images are from three remote sensing data sets: RSOD [52], RSICD [40], and NWPU-RESISC45 [53]. Eight classical methods are selected for comparison: prior-based methods such as DCP [25], CAP [28], NLD [29], and IDeRs [35]; and learning-based methods such as DehazeNet [15], EPDN [19], and MSBDN [59]; and the methods that combine the prior-based method and learning-based method, such as PSD [60]. The source code of these benchmark methods can be downloaded from the author's website, and the configurations strictly follow the authors' suggestions in their articles.

A. Analysis of Accuracy of Atmospheric Veil

According to the atmospheric scattering model, the airlight leads to a color shift in the scene. Therefore, if the estimation of atmospheric veils is inaccurate, then color distortion of the dehazed image occurs. For most studies, the airlight was evaluated by transmission; therefore, we use the refined atmospheric veil to obtain the transmission according to (2).

The accuracy of the atmospheric veil is evaluated by comparing the transmission with other methods. The prior-based methods DCP [25], CAP [28], NLD [29], and IDeRs [35] are selected for comparison, as shown in Fig. 4. According to (5), the transmission should be independent of the texture of the scene in remote sensing images [9]. On the whole, while the edges of the transmission map obtained by our method are preserved and most of the textures are smoothed, other methods still have richer texture details.

In remote sensing images, different objects on the surface of the earth usually have different surface reflection coefficients, thus showing different color saturations. Low saturation is caused not only by haze but also possibly by light-colored objects (such as white or gray buildings, snow, and thin clouds) or translucent coverings. Therefore, the gray airport road in Fig. 3(a) should have a low transmission.

We can see that, compared with our method, the transmissions of the gray airport road obtained by DCP [25], cap [28], and NLD [29] are higher, while the corresponding transmission obtained by IDeRs [35] is lower. This leads to color distortion of the dehazed images, as shown in Fig. 5.

B. Qualitative Evaluation

1) Dehazing Performances With Different Haze Density: We select remote sensing images with different haze densities, including homogeneous haze, heterogeneous haze, and thick haze, for experiments. The results are shown in Figs. 5–7.

In Fig. 5, the results of DCP [25], CAP [28], DehazeNet [15], and EPDN [19] look dim with unclear details. IDeRs [35], NLD [29], and PSD [60] have abundant details but with color distortion, while MSBDN [59] has better color retention but unclear details. The proposed method can keep the color visually consistent with the real scene and abundant distinguishable details. This shows that the proposed LSP can accurately estimate the atmospheric veil and atmospheric light.

For heterogeneous hazy images, all of the methods achieve good dehazed results. Compared with other methods, the proposed method can obtain dehazed images with richer and clearer details, such as the area marked by the red rectangles in Fig. 6. The effectiveness of the proposed method adopts the adaptive radius of the guided filter to refine the atmospheric veil.

In Fig. 7, the entire image is covered with thick haze, making most of the image details invisible. The DCP [25], CAP [28], DehazeNet [15], and MSBDN [59] methods tend to leave haze in the results. The results of NLD [29] and EPDN [19] look dim, while the results of IDeRs [35] and

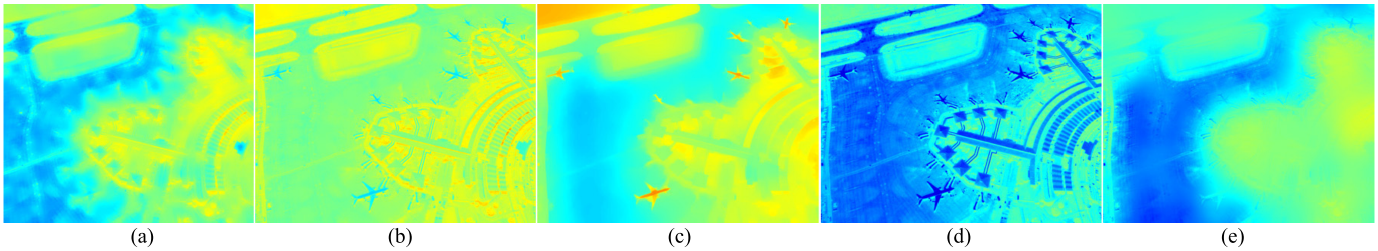

Fig. 4. The transmission estimation. (a) DCP [25]. (b) CAP [28]. (c) NLD [29]. (d) IDeRs [35]. (e) Our method.

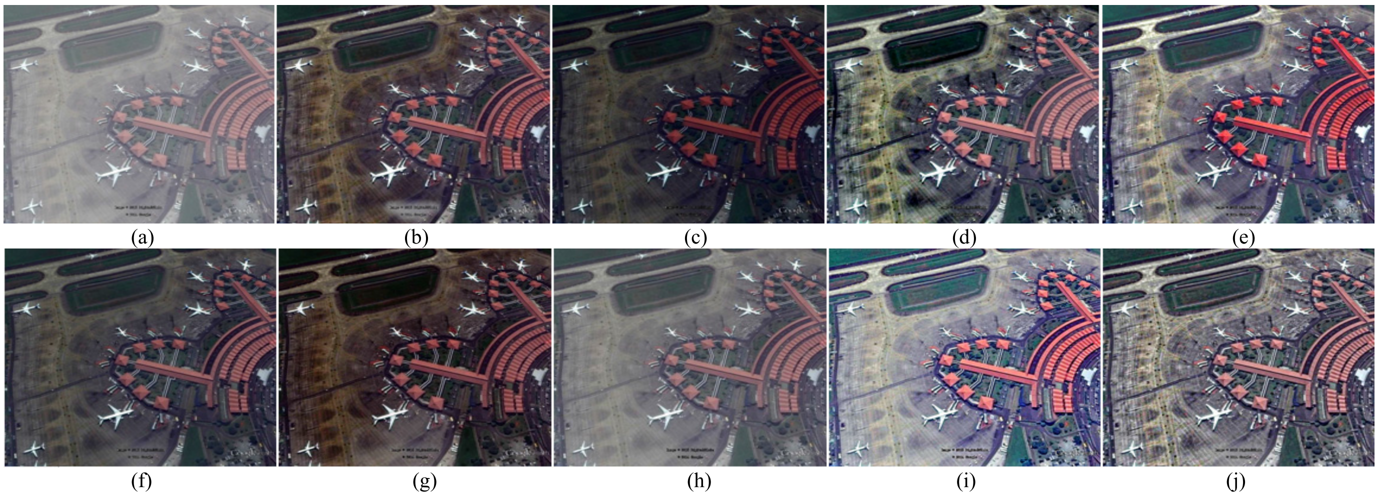

Fig. 5. Dehazed results of different methods on homogeneous haze. (a) Input hazy images. (b) DCP [25]. (c) CAP [28]. (d) NLD [29]. (e) IDeRs [35]. (f) DehazeNet [15]. (g) EPDN [19]. (h) MSBDN [59]. (i) PSD [60]. (j) Our method.

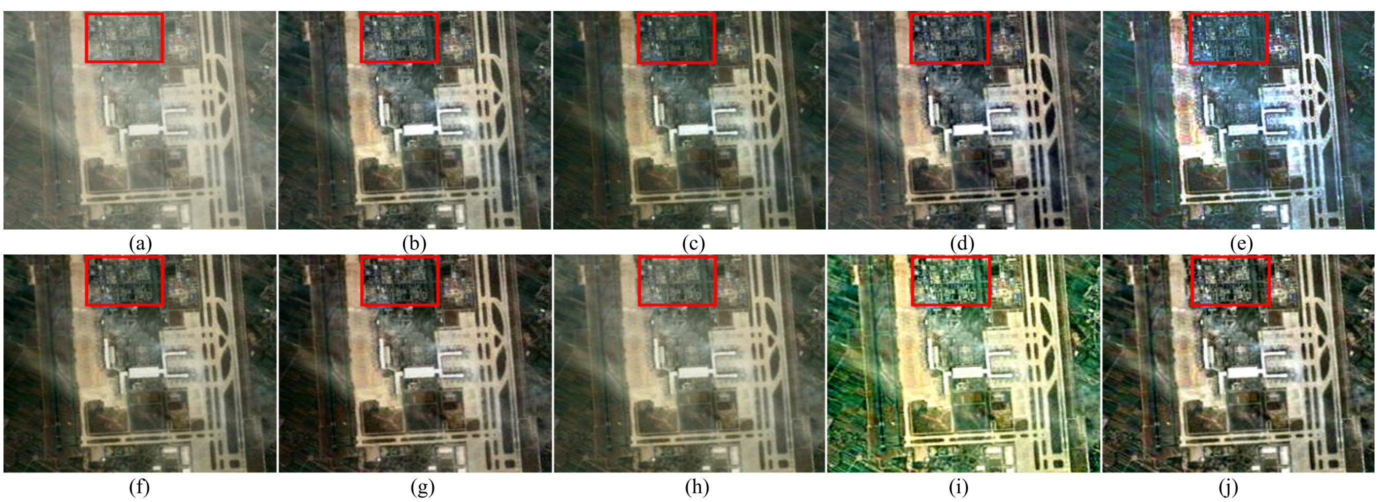

Fig. 6. Dehazed results of different methods on heterogeneous haze. (a) Input hazy images. (b) DCP [25]. (c) CAP [28]. (d) NLD [29]. (e) IDeRs [35]. (f) DehazeNet [15]. (g) EPDN [19]. (h) MSBDN [59]. (i) PSD [60]. (j) Our method.

PSD [60] show saturated color in local regions due to excessive dehazing. The proposed method obtains high-quality dehazed images with high contrast, minimal halo artifacts, and low color distortion.

2) Dehazing Performances With Different Colors: The difference in image color complexity may affect the dehazed results; therefore, we choose three groups of remote sensing images from the above-mentioned three remote sensing data sets. The colors of the remote sensing images are monotonous, as shown in Fig. 8. The colors of remote sensing images are rich, as shown in Fig. 9. The remote sensing images contain white regions, as shown in Fig. 10. White regions often interfere with the selection of atmospheric light; therefore, many existing dehazing methods are sensitive to white light.

Although the DCP [25] and NLD [29] methods show good performance on hazy remote sensing images of monotonous

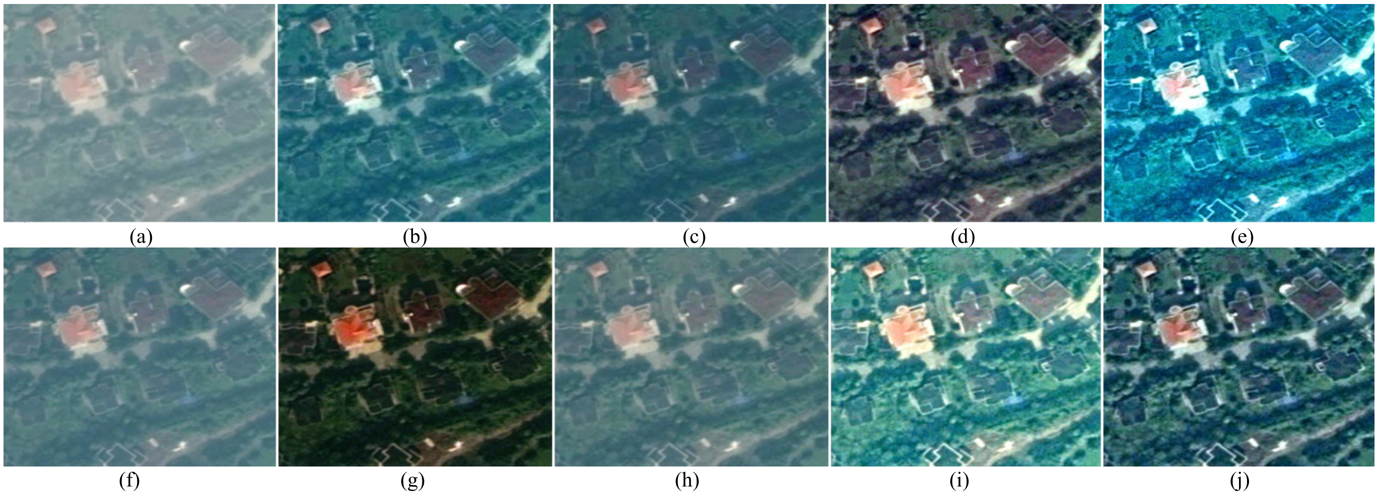

Fig. 7. Dehazed results of different methods on thick haze. (a) Input hazy images. (b) DCP [25]. (c) CAP [28]. (d) NLD [29]. (e) IDeRs [35]. (f) DehazeNet [15]. (g) EPDN [19]. (h) MSBDN [59]. (i) PSD [60]. (j) Our method.

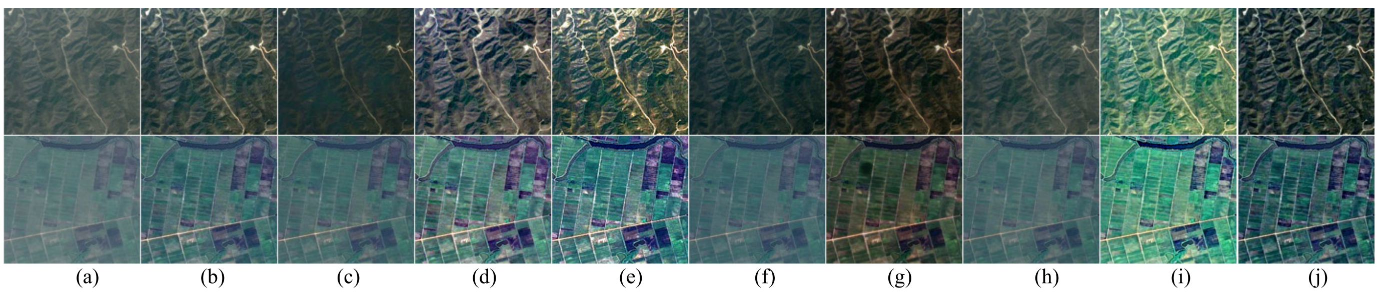

Fig. 8. Dehazed results with different methods on monotonous color images. (a) Input hazy images. (b) DCP [25]. (c) CAP [28]. (d) NLD [29]. (e) IDeRs [35]. (f) DehazeNet [15]. (g) EPDN [19]. (h) MSBDN [59]. (i) PSD [60]. (j) Our method.

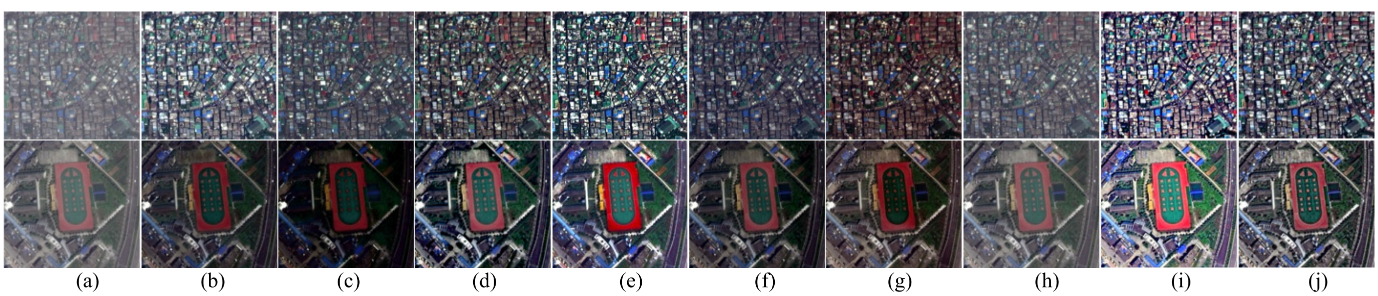

Fig. 9. Dehazed results with different methods on rich color images. (a) Input hazy images. (b) DCP [25]. (c) CAP [34]. (d) NLD [29]. (e) IDeRs [35]. (f) DehazeNet [15]. (g) EPDN [19]. (h) MSBDN [59]. (i) PSD [60]. (j) Our method.

and rich colors that have good color fidelity, they are less robust for remote sensing images with white regions, as illustrated in the first lines of Fig. 10(d) and (h); they are too dark to see the details. Although the dehazed results by IDeRs [35] and PSD [60] are satisfactory in processing details as well as image contrast, they tend to overenhance the image with obvious color distortion and oversaturation [especially in Fig. 9(e)]. The dehazed results of CAP [28], DehazeNet [15], and MSBDN [59] are dim or retain much of the haze, which leads to image blurring with bad visual effects. EPDN [19] successfully removes most of the haze, but the dehazed images tend to be dark and exhibit some color shifting.

Whether the color of remote sensing images is monotonous or rich or contains white regions, our dehazed results retain very fine details and high contrast while preserving the color of the original scene because the atmospheric veil estimated by the proposed method can accurately describe the degradation degree of the captured scene. This demonstrates the effectiveness of the proposed method.

We also choose one of the haze-free remote sensing images in Fig. 2 with gray areas for hazing, as shown in Fig. 11(a). Regard the haze-free image as the ground truth. Using the known transmission $t(x)$ and atmospheric light A, according to (1), the simulated hazy image is obtained as shown in Fig. 11(b). Compared to the ground truth, the results of

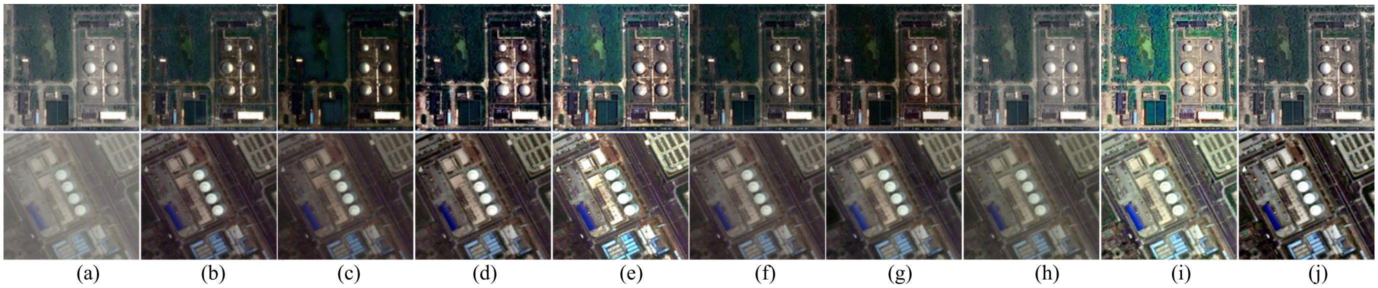

Fig. 10. Dehazed results with different methods on locally white color images. (a) Input hazy images. (b) DCP [25]. (c) CAP [28]. (d) NLD [29]. (e) IDeRs [35]. (f) DehazeNet [15]. (g) EPDN [19]. (h) MSBDN [59]. (i) PSD [60]. (j) Our method.

TABLE I
QUANTITATIVE COMPARISON OF *e* AND *r*

Index		DCP	CAP	NLD	IDeRs	DehazeNet	EPDN	MSBDN	PSD	Ours
Different haze density	e	1.392	1.129	1.468	**1.712**	0.993	1.462	0.297	**1.669**	1.587
	r	1.803	1.183	2.511	**3.605**	1.292	2.067	2.465	**4.729**	3.549
Different colors	e	0.469	0.433	0.464	**0.579**	0.363	0.358	0.105	**0.588**	0.502
	r	1.937	1.126	2.546	**3.706**	1.237	1.761	1.104	**3.871**	3.174
Different scenes	e	0.173	0.245	0.249	**0.269**	0.174	0.029	0.066	**0.266**	0.255
	r	1.589	1.005	2.119	**3.062**	1.138	1.635	1.085	**3.732**	2.791

TABLE II
QUANTITATIVE COMPARISON OF FIVE CRITERION

Method	VI	RI	VSI	PSNR	SSIM
DCP	0.873	0.934	0.931	**18.646**	0.801
CAP	0.741	0.928	0.917	15.895	0.539
NLD	0.853	0.937	0.869	**18.172**	0.735
IDeRs	0.596	0.923	0.802	11.415	0.392
DehazeNet	0.896	0.912	**0.957**	15.454	0.579
EPDN	0.885	0.951	0.916	13.672	0.593
MSBDN	0.849	0.961	0.941	**18.313**	0.537
PSD	0.747	0.957	0.855	17.399	0.483
Ours	**0.917**	**0.964**	**0.948**	17.734	**0.836**

IDeRs [35] and PSD [60] have rich details, but there are obvious color shifts; the results of DCP [25], DehazeNet [15], and EPDN [19] are generally a little dark; the color fidelity of the results are higher by NLD [29], MSBDN [59], and the proposed method, but the image details of the proposed method are clearer.

3) Dehazing Performances for Different Scenes: We also select five hazy remote sensing images of different scenes from the above-mentioned three remote sensing data sets for experiments: ports, industrial areas, parks, overpasses, and thermal power plants. The dehazed results are shown in Fig. 12. The first column shows hazy images, and the last column shows the dehazed images by our method.

According to the five groups of dehazed results, the DCP [25], CAP [28], DehazeNet [43], EPDN [45], and MSBDN [59] methods often suffer from insufficient dehazing, resulting in dehazed images that are often dark and blurry. The results of IDeRs [35], NLD [29], and PSD [60] have clear details but with local oversaturation and color distortion. It can be observed that the proposed method is outstanding among all tested methods when handling different hazy scenes, which can retain the natural colors and fine structures and obtain higher contrast.

C. Quantitative Evaluation

1) Non-Reference Image Quality Assessment: We choose two objective indicators e and r [54] as the non-reference image quality assessment metrics. The indicator e is used to evaluate the ability of the dehazing method to restore the edge. The indicator r is used to evaluate the quality of the contrast restoration by the dehazing method. Generally, the higher e and r, the better the performance.

For a quantitative comparison, we use the hazy remote sensing images in the three groups of different haze densities, different colors, and different scenes to test and obtain the average of e and r in the three groups of remote sensing images. The statistics for each group are listed in Table I. It can be seen that e and r of the dehazed images of IDeRs [35] and PSD [60] are highest because the dehazed images of IDeRs [35] and PSD [60] have obvious color distortion and overenhancement, which makes the newly visible edges and contrast higher. Except for IDeRs [35] and PSD [60], the values of e and r obtained by our method are higher than those of other methods, indicating that our method performs well on most of the hazy remote sensing images.

2) Reference Image Quality Assessment: The reference image quality evaluation requires a clear image as a reference, which is usually obtained by simulation. Compared with the simulation data sets, BeDDE [55] is a real-world benchmark data set that is used to evaluate dehazing methods. It is more convincing to choose BeDDE [55] for experiments. We select 26 images of Chengdu with different haze densities from BeDDE [55]. Here, we only give the dehazed results of the hazy image chengdu_3.png, as shown in Fig. 13. Even if the image contains the sky region, our method achieves a good visual effect, the contrast is enhanced and the color distortion

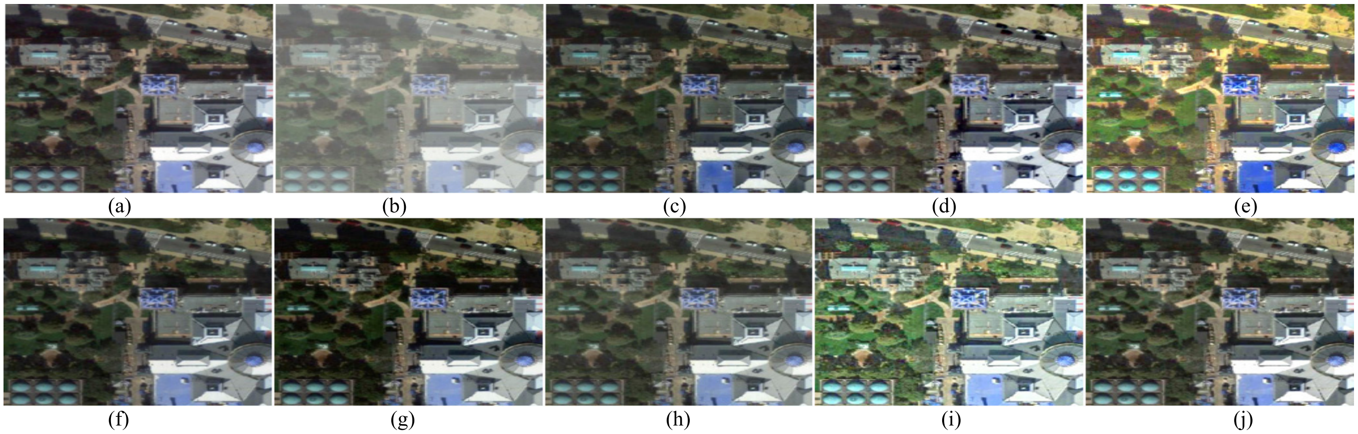

Fig. 11. Dehazed results of a simulated hazy image. (a) Haze-free image. (b) Simulated hazy image. (c) DCP [25]. (d) NLD [29]. (e) IDeRs [35]. (f) DehazeNet [15]. (g) EPDN [19]. (h) MSBDN [59]. (i) PSD [60]. (j) Our method.

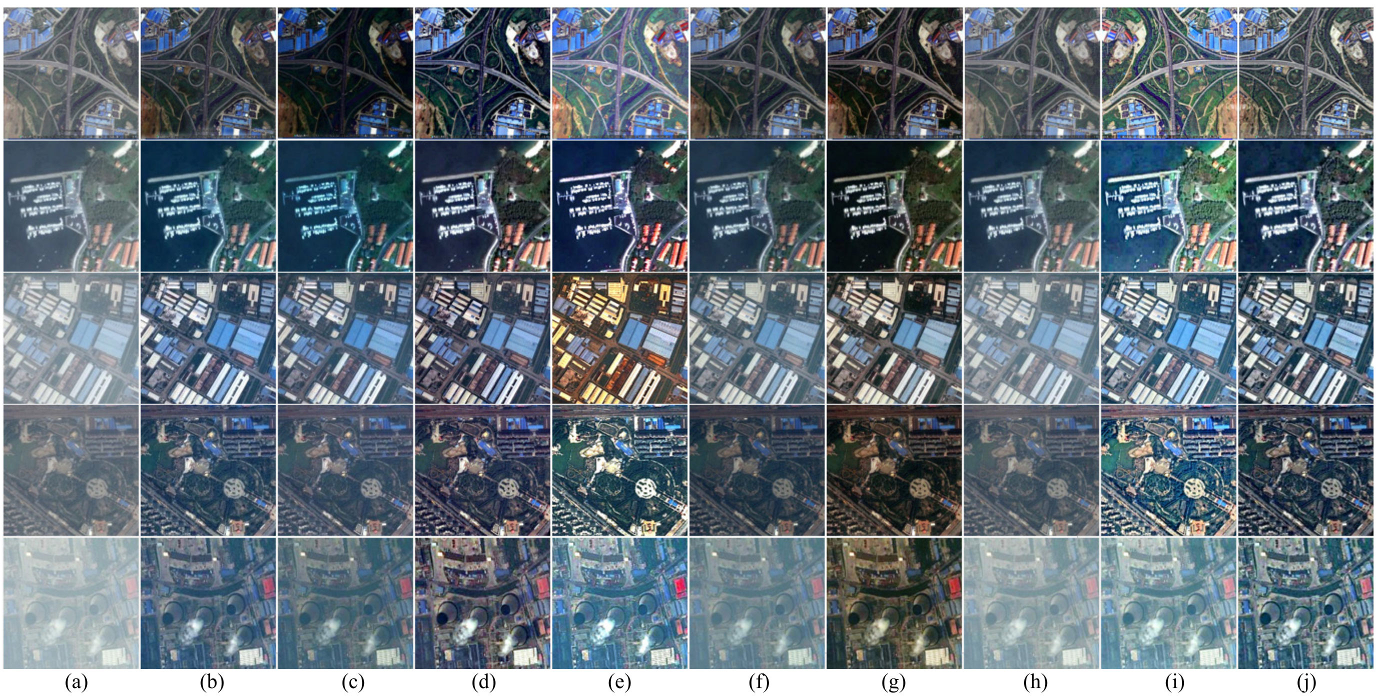

Fig. 12. Dehazed results with different methods on locally white color images. (a) Input hazy images. (b) DCP [25]. (c) CAP [28]. (d) NLD [29]. (e) IDeRs [35]. (f) DehazeNet [15]. (g) EPDN [19]. (h) MSBDN [59]. (i) PSD [60]. (j) Our method.

is not serious. In [55], the sky region is not in the scope of comparison, and the clear image and the mask image are given in [55], as shown in Fig. 13(a) and (f).

We choose five criteria: visibility index (VI) [55], realness index (RI) [55], visual saliency-induced index (VSI) [57], peak-signal-to-noise ratio (PSNR), and structural similarity index measure (SSIM) [58] to evaluate the performance of the dehazing methods, as shown in Table II.

The proposed algorithm obtains the highest values of VI, RI, and SSIM, indicating that the proposed algorithm has obvious advantages in visibility and realness. Although the value of PSNR obtained by the proposed method is slightly lower than that of DCP [25], NLD [29], and MSBDN [59], DCP [25] has an obvious halo; NLD [29] has obvious color distortion; MSBDN [59] has unclear details. DehazeNet [43] has the highest VSI value of 0.957, while the VSI value of the proposed algorithm is 0.948, which is very close to the highest value.

In order to evaluate the color difference (CD) of the dehazing images relative to the ground truth quantitatively, we have selected four methods of quantitative evaluation of color deviation in HSI [66], RGB [65], CIELAB [64], and YC_BC_R [63] color spaces. The four methods are CD1 (Chrominance component CD [67]), CD2 (Adaptive image difference [68]), CD3 (Color image difference [62]), and CD4 (Texture patch CD [61]).

According to the reference image [Fig. 11(a)], the above-mentioned four methods are used to evaluate the CD of the

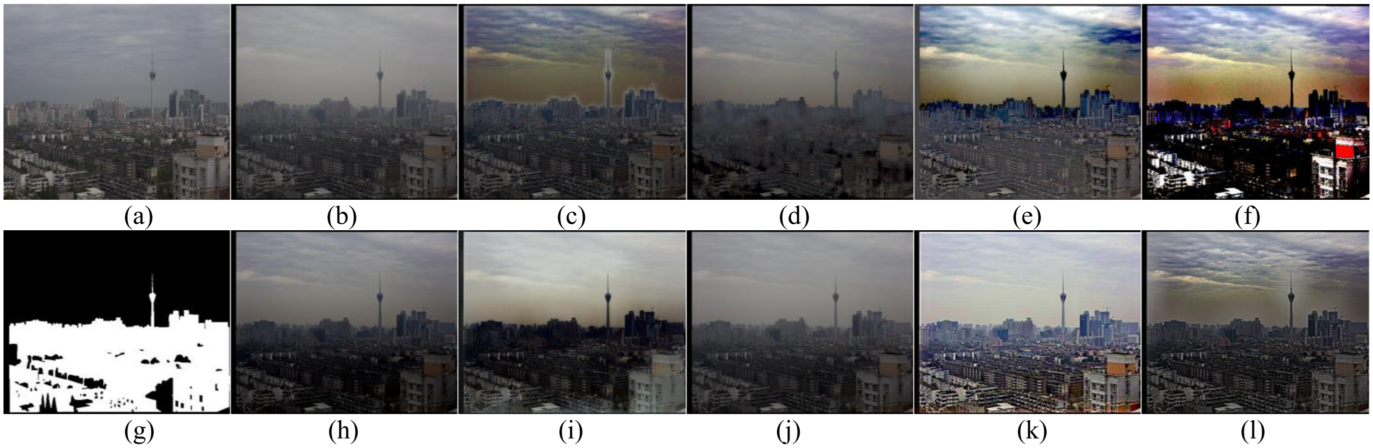

Fig. 13. Experiments on BeDDE data set. (a) Clear image. (b) Input hazy image. (c) DCP [25]. (d) CAP [28]. (e) NLD [29]. (f) Mask image. (g) IDeRs [35]. (h) DehazeNet [15]. (i) EPDN [19]. (j) MSBDN [59]. (k) PSD [60]. (l) Our method.

TABLE III

CD Values for the Image in Fig. 11

Measures	Color spaces	DCP	NLD	IDeRs	DehazeNet	EPDN	MSBDN	PSD	Ours
CD1	HSI	0.573	0.495	**1**	**0.320**	0.818	0.518	0.489	0.492
CD2	RGB	0.747	0.838	**1**	0.693	0.853	**0.566**	0.939	0.690
CD3	CIELAB	0.746	0.771	0.991	0.667	0.929	0.777	**1**	**0.644**
CD4	YC_BC_R	0.261	0.321	**1**	0.216	0.337	0.251	0.643	**0.209**

dehazing images in Fig. 11. Because the data obtained by each method are not in a unified coordinate system, in order to compare the data more clearly, we normalize the data of each group, that is, divide each data by the maximum value of the group; the results obtained are shown in Table III. In this way, the maximum value of each group will be 1, and the larger the value, the greater the CD.

Like our visual perception, IDeRs [35] and PSD [60] have higher values because of the obvious color shifts. Our method achieved the lowest value in the methods of CD3 [62] and CD4 [61]. Although the values obtained in CD1 and CD2 are not the lowest, they are only slightly higher than DehazeNet [43] and MSBDN [59]. It shows that the proposed method maintains the color integrity of the scene after dehazing better than other methods.

V. Conclusion

For single remote sensing image haze removal, we proposed a dehazing method based on an LSP. Considering the overall characteristics of the atmospheric scattering model, the dark channel of a hazy image was decomposed into a sparse dark channel of direct attenuation and a low-rank atmospheric veil. The prior was based on the overall nature of the image; therefore, local pixel changes had no effect on the prior, which effectively enhanced the robustness of the prior.

In addition, the differences between remote sensing images and natural images were fully considered. Considering the different resolutions of remote sensing images, the calculations of patches involved in this article were completed by adaptive methods. The PCP-ADMM method combined with the adaptive threshold shrinkage method was used for low-rank and sparse decomposition to obtain a coarse estimation of the atmospheric veil, and the guided filter with adaptive radius was used to refine it. Considering that there is no sky region in remote sensing images, atmospheric light was estimated by using a refined atmospheric veil. The haze-free image was restored based on the deformed atmospheric scattering model of the atmospheric veil and atmospheric light. Finally, we conducted a large number of tests on remote sensing images with different haze densities, different colors, and different scenes in three public remote sensing data sets and compared them with six advanced qualitative and quantitative methods. The experimental results showed that the dehazed image obtained by the proposed method has rich detail, high contrast, and minimal halo artifacts and color distortion. This result is superior to those of most state-of-the-art methods.

References

[1] C. Liu, L. He, Z. Li, and J. Li, "Feature-driven active learning for hyperspectral image classification," *IEEE Trans. Geosci. Remote Sens.*, vol. 56, no. 1, pp. 341–354, Jan. 2017.

[2] G. Cheng and J. Han, "A survey on object detection in optical remote sensing images," *ISPRS J. Photogramm. Remote Sens.*, vol. 117, pp. 11–28, Jul. 2016.

[3] M. Wang, Y. Wan, Z. Ye, and X. Lai, "Remote sensing image classification based on the optimal support vector machine and modified binary coded ant colony optimization algorithm," *Inf. Sci.*, vol. 402, pp. 50–68, Sep. 2017.

[4] J. A. Stark, "Adaptive image contrast enhancement using generalizations of histogram equalization," *IEEE Trans. Image Process.*, vol. 9, no. 5, pp. 889–896, May 2000.

[5] S. G. Narasimhan and S. K. Nayar, "Contrast restoration of weather degraded images," *IEEE Trans. Pattern Anal. Mach. Learn.*, vol. 25, no. 6, pp. 713–724, Jun. 2003.

[6] J.-Y. Kim, L.-S. Kim, and S.-H. Hwang, "An advanced contrast enhancement using partially overlapped sub-block histogram equalization," *IEEE Trans. Circuits Syst. Video Technol.*, vol. 11, no. 4, pp. 475–484, Apr. 2001.

[7] D. J. Jobson, Z.-U. Rahman, and G. A. Woodell, "A multiscale Retinex for bridging the gap between color images and the human observation of scenes," *IEEE Trans. Image Process.*, vol. 6, no. 7, pp. 965–976, Jul. 1997.

[8] Z.-Ur Rahman, D. J. Jobson, and G. A. Woodell, "Retinex processing for automatic image enhancement," *J. Electron. Imag.*, vol. 13, no. 1, pp. 100–111, Jan. 2004.

[9] X. Pan, F. Xie, Z. Jiang, and J. Yin, "Haze removal for a single remote sensing image based on deformed haze imaging model," *IEEE Signal Process. Lett.*, vol. 22, no. 10, pp. 1806–1810, Oct. 2015.

[10] P. S. Chavez, Jr., "An improved dark-object subtraction technique for atmospheric scattering correction of multispectral data," *Remote Sens. Environ.*, vol. 24, no. 3, pp. 459–479, Apr. 1988.

[11] A. Makarau, R. Richter, R. Müller, and P. Reinartz, "Haze detection and removal in remotely sensed multispectral imagery," *IEEE Trans. Geosci. Remote Sens.*, vol. 52, no. 9, pp. 5895–5905, Sep. 2014.

[12] Y. Zhang, B. Guindon, and J. Cihlar, "An image transform to characterize and compensate for spatial variations in thin cloud contamination of Landsat images," *Remote Sens. Environ.*, vol. 82, nos. 2–3, pp. 173–187, Oct. 2002.

[13] H. Jiang, N. Lu, and L. Yao, "A high-fidelity haze removal method based on HOT for visible remote sensing images," *Remote Sens.*, vol. 8, no. 10, p. 844, Oct. 2016.

[14] Q. Liu, X. Gao, L. He, and W. Lu, "Haze removal for a single visible remote sensing image," *Signal Process.*, vol. 137, pp. 33–43, Aug. 2017.

[15] B. L. Cai, X. M. Xu, K. Jia, C. M. Qing, and D. C. Tao, "Dehazenet: An end-to-end system for single image haze removal," *IEEE Trans. Image Process*, vol. 25, no. 11, pp. 5187–5198, Aug. 2016.

[16] I. Goodfellow *et al.*, "Generative adversarial nets," in *Proc. Adv. Neural Inf. Process. Syst.*, 2014, pp. 2672–2680.

[17] B. Li, X. Peng, Z. Wang, J. Xu, and D. Feng, "AOD-Net: All-in-one dehazing network," in *Proc. IEEE Int. Conf. Comput. Vis. (ICCV)*, Oct. 2017, pp. 4780–4788.

[18] H. Zhang and V. M. Patel, "Densely connected pyramid dehazing network," in *Proc. IEEE/CVF Conf. Comput. Vis. Pattern Recognit.*, Jun. 2018, pp. 3194–3203.

[19] Y. Qu, Y. Chen, J. Huang, and Y. Xie, "Enhanced Pix2Pix dehazing network," in *Proc. IEEE/CVF Conf. Comput. Vis. Pattern Recognit. (CVPR)*, Long Beach, CA USA, Jun. 2019, pp. 8160–8168.

[20] H. Jiang and N. Lu, "Multi-scale residual convolutional neural network for haze removal of remote sensing images," *Remote Sens.*, vol. 10, no. 6, p. 945, 2018.

[21] A. Hu, Z. Xie, Y. Xu, M. Xie, L. Wu, and Q. Qiu, "Unsupervised haze removal for high-resolution optical remote-sensing images based on improved generative adversarial networks," *Remote Sens.*, vol. 12, no. 24, p. 4162, Dec. 2020.

[22] Z. Gu, Z. Zhan, Q. Yuan, and L. Yan, "Single remote sensing image dehazing using a prior-based dense attentive network," *Remote Sens.*, vol. 11, no. 24, p. 3008, Dec. 2019.

[23] W. T. Chen, J.-J. Ding, and S. Y. Kuo, "PMS-Net: Robust haze removal based on patch map for single images," in *Proc. IEEE/CVF Conf. Comput. Vis. Pattern Recognit. (CVPR)*, Jun. 2019, p. 11.

[24] J. P. Tarel, N. Hautiere, L. Caraffa, A. Cord, H. Halmaoui, and D. Gruyer, "Vision enhancement in homogeneous and heterogeneous fog," *IEEE Intell. Transp. Syst. Mag.*, vol. 4, no. 2, pp. 6–20, Apr. 2012.

[25] D. Makkar and M. Malhotra, "Single image haze removal using dark channel prior," *Int. J. Eng. Comput. Sci.*, pp. 1956–1963, Jan. 2016.

[26] G. L. Bi, J. Y. Ren, T. J. Fu, T. Nie, C. Z. Chen, and N. Zhang, "Image dehazing based on accurate estimation of transmission in the atmospheric scattering model," *IEEE Photon. J.*, vol. 9, no. 4, pp. 1–18, Aug. 2017.

[27] S. G. Narasimhan and S. K. Nayar, "Vision and the atmosphere," *Int. J. Comput. Vis.*, vol. 48, no. 3, pp. 233–254, 2002.

[28] Q. Zhu, J. Mai, and L. Shao, "A fast single image haze removal algorithm using color attenuation prior," *IEEE Trans. Image Process.*, vol. 24, no. 11, pp. 3522–3533, Nov. 2015.

[29] D. Berman, T. Treibitz, and S. Avidan, "Non-local image dehazing," in *Proc. IEEE Conf. Comput. Vis. Pattern Recognit. (CVPR)*, Jun. 2016, pp. 1674–1682.

[30] J. Shin *et al.*, "Radiance-reflectance combined optimization and structure-guided ℓ_0-norm for single image dehazing," *IEEE Trans. Multimedia*, vol. 22, no. 1, pp. 30–44, Jan. 2020.

[31] H.-M. Hu, H. Zhang, Z. Zhao, B. Li, and J. Zheng, "Adaptive single image dehazing using joint local-global illumination adjustment," *IEEE Trans. Multimedia*, vol. 22, no. 6, pp. 1485–1495, Jun. 2020.

[32] T. M. Bui and W. Kim, "Single image dehazing using color ellipsoid prior," *IEEE Trans. Image Process.*, vol. 27, no. 2, pp. 999–1009, Feb. 2018.

[33] J. Long, Z. Shi, W. Tang, and C. Zhang, "Single remote sensing image dehazing," *IEEE Geosci. Remote Sens. Lett.*, vol. 11, no. 1, pp. 59–63, Jan. 2014.

[34] Q. Guo, H.-M. Hu, and B. Li, "Haze and thin cloud removal using elliptical boundary prior for remote sensing image," *IEEE Trans. Geosci. Remote Sens.*, vol. 57, no. 11, pp. 9124–9137, Nov. 2019.

[35] L. Xu, D. Zhao, Y. Yan, S. Kwong, J. Chen, and L.-Y. Duan, "IDeRs: Iterative dehazing method for single remote sensing image," *Inf. Sci.*, vol. 489, pp. 50–62, Jul. 2019.

[36] J. P. Tarel, "Fast visibility restoration from a single color or gray level image," in *Proc. IEEE 12th Int. Conf. Comput. Vis.*, Sep. 2010, pp. 2201–2208.

[37] J. Yu, D.-P. Li, and Q.-M. Liao, "Physics-based fast single image fog removal," *Acta Automatica Sinica*, vol. 37, no. 2, pp. 143–149, Jun. 2011.

[38] D. Yang and J. Sun, "Proximal Dehaze-Net: A prior learning-based deep network for single image dehazing," in *Proc. IEEE Int. Conf. Comput. Vis.*, Sep. 2018, pp. 729–746.

[39] L. J. Zhao. (2015). *RS_C11_Database*. Jan. 15, 2016. [Online]. Available: https://www. researchgate.net/publication/271647282_RS_C11_Database

[40] X. Lu, B. Wang, X. Zheng, and X. Li, "Exploring models and data for remote sensing image caption generation," *IEEE Trans. Geosci. Remote Sens.*, vol. 56, no. 4, pp. 2183–2195, Apr. 2018.

[41] E. Candés, X. Li, Y. Ma, and J. Wright, "Robust principal component analysis?: Recovering low-rank matrices from sparse errors," in *Proc. IEEE Sensor Array Multichannel Signal Process. Workshop*, vol. 8, no. 1, Oct. 2010, pp. 201–204.

[42] Z. Kang, C. Peng, and Q. Cheng, "Robust PCA via nonconvex rank approximation," in *Proc. IEEE Int. Conf. Data Mining*, Nov. 2015, pp. 211–220.

[43] F. Cao, J. Chen, H. Ye, J. Zhao, and Z. Zhou, "Recovering low-rank and sparse matrix based on the truncated nuclear norm," *Neural Netw.*, vol. 85, pp. 10–20, Jan. 2017.

[44] M. Fornasier and H. Rauhut, "Iterative thresholding algorithms," *Appl. Comput. Harmon. Anal.*, vol. 25, no. 2, pp. 187–208, 2008.

[45] W. Zuo and Z. Lin, "A generalized accelerated proximal gradient approach for total-variation-based image restoration," *IEEE Trans. Image Process.*, vol. 20, no. 10, pp. 2748–2759, Oct. 2011.

[46] A. Chambolle and T. Pock, "A first-order primal-dual algorithm for convex problems with applications to imaging," *J. Math. Imag. Vis.*, vol. 40, no. 1, pp. 120–145, 2011.

[47] M.-S. Kim and D.-H. Choi, "A new penalty parameter update rule in the augmented Lagrange multiplier method for dynamic response optimization," *KSME Int. J.*, vol. 14, no. 10, pp. 1122–1130, 2000.

[48] S. Boyd, N. Parikh, E. Chu, B. Peleato, and J. Eckstein, "Distributed optimization and statistical learning via the alternating direction method of multipliers," *Found. Trends Mach. Learn.*, vol. 3, no. 1, pp. 1–122, Nov. 2010.

[49] Y. Xiao, L. Chen, and D. Li, "A generalized alternating direction method of multipliers with semi-proximal terms for convex composite conic programming," *Math. Program. Comput.*, vol. 10, no. 4, pp. 533–555, Dec. 2018.

[50] D. L. Donohn, "Denoising by soft thresholding," *IEEE Trans. Inf. Theory*, vol. 41, no. 3, pp. 613–617, Mar. 1995.

[51] K. He, J. Sun, and X. Tang, "Guided image filtering," *IEEE Trans. Pattern Anal. Mach. Intell.*, vol. 35, no. 6, pp. 1397–1409, Jun. 2013.

[52] Y. Long, Y. Gong, Z. Xiao, and Q. Liu, "Accurate object localization in remote sensing images based on convolutional neural networks," *IEEE Trans. Geosci. Remote Sens.*, vol. 55, no. 5, pp. 2486–2498, May 2017.

[53] G. Cheng, J. Han, and X. Lu, "Remote sensing image scene classification: Benchmark and state of the art," *Proc. IEEE*, vol. 105, no. 10, pp. 1865–1883, Oct. 2017.

[54] N. Hautiere, J. P. Tarel, D. Aubert, and E. Dumont, "Blind contrast enhancement assessment by gradient ratioing at visible edges," *Image Anal. Stereol.*, vol. 27, no. 1, pp. 87–95, 2008.

[55] S. Zhao, L. Zhang, S. Huang, Y. Shen, and S. Zhao, "Dehazing evaluation: Real-world benchmark datasets, criteria, and baselines," *IEEE Trans. Image Process.*, vol. 29, pp. 6947–6962, 2020.

[56] G. Bi, L. Wang, C. Chen, X. Zhang, and G. Li, "Fast single-image dehazing algorithm based on piecewise transformation in optical model," *IEEE Photon. J.*, vol. 13, no. 2, pp. 1–19, Apr. 2021.
[57] L. Zhang, Y. Shen, and H. Li, "VSI: A visual saliency-induced index for perceptual image quality assessment," *IEEE Trans. Image Process.*, vol. 23, no. 10, pp. 4270–4281, Oct. 2014.
[58] Z. Wang, A. C. Bovik, H. R. Sheikh, and E. P. Simoncelli, "Image quality assessment: From error visibility to structural similarity," *IEEE Trans. Image Process.*, vol. 13, no. 4, pp. 600–612, Apr. 2004.
[59] H. Dong *et al.*, "Multi-scale boosted dehazing network with dense feature fusion," in *Proc. IEEE/CVF Conf. Comput. Vis. Pattern Recognit. (CVPR)*, Jun. 2020, pp. 2157–2167.
[60] Z. Chen, Y. Wang, Y. Yang, and D. Liu, "PSD: Principled synthetic-to-real dehazing guided by physical priors," in *Proc. IEEE/CVF Conf. Comput. Vis. Pattern Recognit. (CVPR)*, Jun. 2021, pp. 7180–7189.
[61] B. Ortiz-Jaramillo, A. Kumcu, L. Platisa, and W. Philips, "Evaluation of color differences in natural scene color images," *Signal Process., Image Commun.*, vol. 71, p. 128- 137, Feb. 2019.
[62] I. Lissner, J. Preiss, P. Urban, M.-S. Lichtenauer, and P. Zolliker, "Image-difference prediction: From grayscale to color," *IEEE Trans. Image Process.*, vol. 22, no. 2, pp. 435–446, Sep. 2013.
[63] (1995). *Recommendation ITU-R BT.601-5 Studio Encoding Parameters of Digital Television for Standard 4:3 and Wide-Screen 16:9 Aspect Ratios*. [Online]. Available: https://www.itu.int/dms_pubrec/itu-r/rec/bt/R-REC-BT.601-5-199510-S!!PDF-E.pdf.
[64] (1976). *CIE, Colorimetry—Part 4: CIE 1976 L*a*b* Colour Space*. [Online]. Available: https://www.iso.org/obp/ui/#iso: std: iso:11664:-4: ed-1: v1: en
[65] G. Sharma, *Digital Color Imaging Handbook* (Color Fundamentals for Digital Imaging). Boca Raton, FL, USA: CRC Press, 2002.
[66] A. Smith, "Color GAMUT transform pairs," *Comput. Graph.*, vol. 12, pp. 12–19, Aug. 1978.
[67] M. Yu, H. Liu, Y. Guo, and D. Zhao, "A method for reduced-reference color image quality assessment," in *Proc. 2nd Int. Congr. Image Signal Process.*, Oct. 2009, pp. 1–5.
[68] U. Rajashekar, Z. Wang, and E. P. Simoncelli, "Quantifying color image distortions based on adaptive spatio-chromatic signal decompositions," in *Proc. 16th IEEE Int. Conf. Image Process. (ICIP)*, Nov. 2009, pp. 2213–2216.

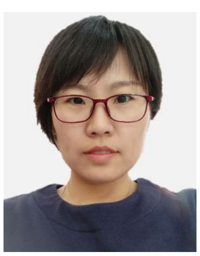

Guoling Bi received the Ph.D. degree in mechanical and electronic engineering from the University of Chinese Academy of Sciences, Beijing, China, in 2015.

She is currently an Associate Professor with the Changchun Institute of Optics, Fine Mechanics and Physics, Chinese Academy of Sciences, Changchun, China. She has authored or coauthored more than 30 articles in academic journals and conferences, and has obtained eight national invention patents. Her main research interests include computer vision, pattern recognition, intelligent computing, and information processing.

Dr. Bi is currently a reviewer for Acta Physica Sinica.

Guoliang Si received the B.S. degree from Jilin University, Changchun, China, in 2001.

He is currently an Associate Professor with the Changchun Institute of Optics, Fine Mechanics and Physics, Chinese Academy of Sciences, Changchun. His research direction is mainly for the design of large-scale integrated circuits and the hardware implementation of image processing algorithms.

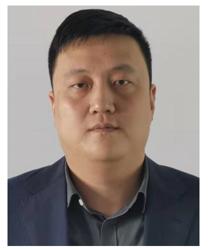

Yuchen Zhao received the Ph.D. degree from the Changchun Institute of Optics, Fine Mechanics and Physics, Chinese Academy of Sciences, Changchun, China, in 2016.

He joined the Changchun Institute of Optics, Fine Mechanics and Physics, Chinese Academy of Sciences, in 2016, where he had been engaged in optical design.

Dr. Zhao is currently a reviewer for infrared and laser engineering.

Biao Qi received the B.S. degree in automation from Harbin Engineering University, Harbin, China, in 2015, and the M.S. degree in control engineering from the Harbin Institute of Technology, Harbin, in 2017. He is currently pursuing the Ph.D. degree with the University of Chinese Academy of Sciences, Beijing, China.

He is currently a Research Associate with the Changchun Institute of Optics, Fine Mechanics and Physics, Chinese Academy of Sciences, Changchun, China, where he majors in image processing and image fusion.

Hengyi Lv received the B.S. degree in automation from the Dalian University of Technology, Dalian, China, in 2007, the M.S. degree in automatic control from the Harbin Institute of Technology, Harbin, China, in 2009, and the Ph.D. degree in mechatronic engineering from the University of Chinese Academy of Sciences, Beijing, China, in 2018.

He is currently an Associate Research Fellow and a Ph.D. Supervisor with the Changchun Institute of Optics, Fine Mechanics and Physics, Chinese Academy of Sciences, Beijing. His research interests include electronics of space camera, space remote sensing imaging technology, dynamic vision sensor application, and artificial intelligence (AI) advanced imaging technology.